ARTICLE

Frustrated spin order and stripe fluctuations in FeSe

A. Baum [1,2], H.N. Ruiz[3,4], N. Lazarević[5], Yao Wang [3,6,10], T. Böhm[1,2,11], R. Hosseinian Ahangharnejhad[1,2,12], P. Adelmann[7], T. Wolf[7], Z.V. Popović[5,8], B. Moritz[3], T.P. Devereaux[3,9] & R. Hackl [1]

The charge and spin dynamics of the structurally simplest iron-based superconductor, FeSe, may hold the key to understanding the physics of high temperature superconductors in general. Unlike the iron pnictides, FeSe lacks long range magnetic order in spite of a similar structural transition around 90 K. Here, we report results of Raman scattering experiments as a function of temperature and polarization and simulations based on exact diagonalization of a frustrated spin model. Both experiment and theory find a persistent low energy peak close to 500 cm^{-1} in B_{1g} symmetry, which softens slightly around 100 K, that we assign to spin excitations. By comparing with results from neutron scattering, this study provides evidence for nearly frustrated stripe order in FeSe.

[1] Walther Meissner Institut, Bayerische Akademie der Wissenschaften, 85748 Garching, Germany. [2] Fakultät für Physik E23, Technische Universität München, 85748 Garching, Germany. [3] Stanford Institute for Materials and Energy Sciences, SLAC National Accelerator Laboratory, 2575 Sand Hill Road, Menlo Park, CA 94025, USA. [4] Department of Physics, Stanford University, Stanford, CA 94305, USA. [5] Center for Solid State Physics and New Materials, Institute of Physics Belgrade, University of Belgrade, Pregrevica 118, 11080 Belgrade, Serbia. [6] Department of Applied Physics, Stanford University, Stanford, CA 94305, USA. [7] Karlsruher Institut für Technologie, Institut für Festkörperphysik, 76021 Karlsruhe, Germany. [8] Serbian Academy of Sciences and Arts, Knez Mihailova 35, 11000 Belgrade, Serbia. [9] Geballe Laboratory for Advanced Materials, Stanford University, Stanford, CA 94305, USA. [10] Present address: Lyman Laboratory 336, Harvard University, 17 Oxford St. Cambridge, 02138 MA, USA. [11] Present address: TNG Technology Consulting GmbH, Beta-Straße, 85774 Unterföhring, Germany. [12] Present address: School of Solar and Advanced Renewable Energy, Department of Physics and Astronomy, University of Toledo, Toledo, OH 43606, USA. Correspondence and requests for materials should be addressed to R.H. (email: hackl@wmi.badw.de)

F e-based pnictides and chalcogenides, similar to cuprates, manganites or some heavy fermion compounds, are characterized by the proximity and competition of various phases including magnetism, charge order, and superconductivity. Specifically the magnetism of Fe-based systems has various puzzling aspects which do not straightforwardly follow from the Fe valence or changes in the Fermi surface topology[1–4]. Some systems have a nearly ordered localized moment close to $2\mu_B$[5], such as FeTe or rare-earth iron selenides, whereas the moments of $A\mathrm{Fe_2As_2}$-based compounds (A = Ba, Sr, Eu or Ca) are slightly below $1\mu_B$[6] and display aspects of itinerant spin-density-wave (SDW) magnetism with a gap in the electronic excitation spectrum[7]. In contrast others do not order down to the lowest temperatures, such as FeSe[8] or LaFePO[9].

The material specific differences are a matter of intense discussion, and low- as well as high-energy electronic and structural properties determine the properties[1,2,4,10–13]. At the Fermi energy E_F, the main fraction of the electronic density of states originates from t_{2g} Fe orbitals, but a substantial part of the Fe–Fe hopping occurs via the pnictogen or chalcogen atoms, hence via the xz, yz, and p_z orbitals. For geometrical reasons, the resulting exchange coupling energies between nearest (J_1) and next nearest neighbor (J_2) iron atoms have the same order of magnitude, and small changes in the pnictogen (chalcogen) height above the Fe plane influence the ratio J_2/J_1, such that various orders are energetically very close[12].

The reduced overlap of the in-plane xy orbitals decreases the hopping integral t and increases the influence of the Hund's rule interactions and the correlation energy U, even though they are only in the range of 1–2 eV. Thus the electrons in the xy orbitals have a considerably higher effective mass m^* and smaller quasiparticle weight Z than those of the xz and yz orbitals. This effect was coined orbital selective Mottness[14–16] and was observed by photoemission spectroscopy (ARPES) in Fe-based chalcogenides[17]. It is similar in spirit to what was found by Raman scattering in the cuprates as a function of momentum[18]. In either case some of the electron wave functions are more localized than others. This paradigm may explain why the description remains difficult and controversial in all cases.

Therefore we address the question as to whether systematic trends can be found across the families of the Fe-based superconductors, how the spin excitations are related to other highly correlated systems, and how they can be described appropriately.

As an experimental tool we use Raman scattering since the differences expected theoretically[1,3] and indicated experimentally in the electronic structure[7] can be tracked in both the charge and the spin channel. Another advantage is the large energy range of approximately 1 meV to 1 eV (8–8000 cm^{-1}) accessible by light scattering[19].

Early theoretical work on Fe-based systems considered the Heisenberg model the most appropriate approach[20], and the high-energy maxima observed by Raman scattering in $\mathrm{BaFe_2As_2}$ were interpreted in terms of localized spins[21,22]. On the other hand, the low-energy spectra are reminiscent of charge density wave (CDW) or SDW formation[22–25]. In principle, both effects can coexist if the strength of the correlations varies for electrons from different orbitals, where itinerant electrons form a SDW, while those on localized orbitals give rise to a Heisenberg-like response.

In contrast to the $A\mathrm{Fe_2As_2}$-based compounds, FeSe seems to be closer to localized order with a larger mass renormalization than in the iron pnictides[1]. Apart from low lying charge excitations, the remaining, presumably spin, degrees of freedom in FeSe may be adequately described by a spin-1 J_1-J_2-J_3-K Heisenberg model[12] which provides also a consistent description of our results shown in this work and allows for the presence of different spin orders. Since various types of spin order are energetically in close proximity[12,26,27], frustration may quench long-range order down to the lowest temperatures[8], even though neutron scattering experiments in FeSe find large values for the exchange energies[27,28].

Recent experiments on FeSe focused on low-energies and B_{1g} ($x^2 - y^2$) symmetry, and the response was associated with particle-hole excitations and critical fluctuations[29]. Here, we obtain similar experimental results below 1500 cm^{-1}. Those in the range 50–200 cm^{-1} show similarities with the other Fe-based systems while those above 200 cm^{-1} are distinctly different but display similarities with the cuprates[30,31]. In addition to previous work, we analyze all symmetries at higher energies up to 3500 cm^{-1}, to uncover crucial information about the behavior of the spin degrees of freedom.

By comparing experimental and simulated Raman data we find a persistent low-energy peak at roughly 500 cm^{-1} in B_{1g} symmetry, which softens slightly around 100 K. We assign the B_{1g} maximum and the related structures in A_{1g} and B_{2g} symmetry to spin excitations. The theoretical simulations also aim at establishing a link between light and neutron scattering data with respect to the spin degrees of freedom and to furnish evidence for nearly frustrated stripe order at low temperature. We arrive at the conclusion that frustrated order of localized spins dominates the physics in FeSe, while critical spin and/or charge fluctuations are not the main focus of the paper.

Results

Experiments. Symmetry-resolved Raman spectra of single-crystalline FeSe (see Methods) in the energy range up to 0.45 eV (3600 cm^{-1}) are shown in Fig. 1. The spectra are linear combinations of the polarization dependent raw data (see Methods and Supplementary Fig. 1 in Supplementary Note 1). For B_{1g} symmetry (Fig. 1a) we plot only two temperatures, 40 and 300 K, to highlight the persistence of the peak at ~500 cm^{-1}. The full temperature dependence will be shown below. For A_{1g}, A_{2g}, and B_{2g} symmetry we show spectra at 40, 90, and 300 K (Fig. 1b–d). Out of the four symmetries, the A_{1g}, B_{1g}, and B_{2g} spectra display Raman active phonons, magnons or electron-hole excitations, while the A_{2g} spectra are weak and vanish below 500–1000 cm^{-1}. As intensity in A_{2g} symmetry appears only under certain conditions not satisfied in the present study, we ignore it here.

In the high-energy limit the intensities are smaller in all symmetries than those in other Fe-based systems such as $\mathrm{BaFe_2As_2}$ (see Supplementary Fig. 2 in Supplementary Note 2). However, in the energy range up to ~3000 cm^{-1} there is a huge additional contribution to the B_{1g} cross section in FeSe (Fig. 1a). The response is strongly temperature dependent and peaks at 530 cm^{-1} in the low-temperature limit. Between 90 and 40 K the A_{1g} and B_{2g} spectra increase slightly in the range around 700 and 3000 cm^{-1}, respectively (indicated as blue shaded areas in Fig. 1b, d). The overall intensity gain in the A_{1g} and B_{2g} spectra in the shaded range is a fraction of ~5% of that in B_{1g} symmetry. The B_{2g} spectra exhibit a reduction in spectral weight in the range from 600 to 1900 cm^{-1} (shaded red) which is already fully developed at the structural transition at $T_s = 89.1$ K in agreement with earlier work[29]. In contrast to A_{1g} and B_{2g} symmetry, the temperature dependence of the B_{1g} intensity is strong, whereas the peak energy changes only weakly, displaying some similarity with the cuprates[32]. This similarity, along with the considerations of Glasbrenner et al.[12], motivated us to explore a spin-only, Heisenberg-like model for describing the temperature evolution of the Raman scattering data.
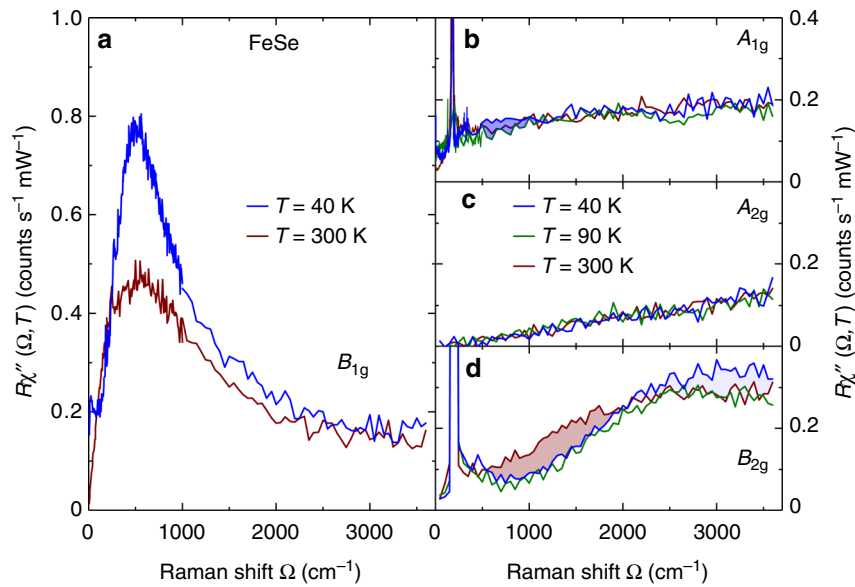
Fig. 1 Symmetry-resolved Raman spectra of FeSe at various temperatures for large energy transfers. **a** B_{1g} spectra at temperatures as indicated. The spectrum at 90 K is omitted here for clarity but is displayed in a separate figure below The weak structure at $T = 40$ K in the range 20–25 cm^{-1} is left over from the fluctuation peak which is most pronounced right above T_s as shown below. **b** A_{1g}, **c** A_{2g}, and **d** B_{2g} spectra at temperatures as indicated. In A_{1g} and B_{2g} symmetry particle-hole excitations dominate the response. In agreement with the simulations weak additional peaks from spin excitations appear at low temperature (blue shaded areas). B_{2g} shows a loss of spectral weight (shaded red). The narrow lines close to 200 cm^{-1} are the A_{1g} and B_{1g} phonons. In the 1 Fe unit cell used here the B_{1g} phonon appears in B_{2g} symmetry since the axes are rotated by 45° with respect to the crystallographic (2 Fe) cell. The A_{2g} intensity vanishes below 500 cm^{-1} and the cross section is completely temperature independent
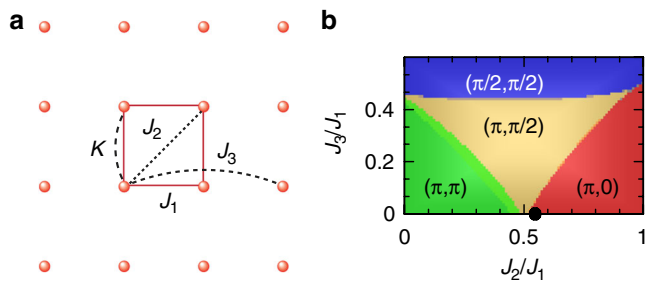

Fig. 2 Model and resulting phase diagram. **a** A 4 × 4 cluster was used for the simulations. The red spheres represent the Fe atoms, each of which carries localized spin $\mathbf{S}_i$, with $S = 1$. The nearest, next-nearest, and next-next-nearest neighbor interactions J_1, J_2, and J_3, respectively, are indicated. K is the coefficient of the biquadratic term proportional to $(\mathbf{S}_i \cdot \mathbf{S}_j)^2$. **b** $J_2 - J_3$ phase diagram as obtained from our simulations at $T = 0$ and for $K = 0.1$. The black dot shows the parameters at which temperature-dependent simulations have been performed

Simulations at zero temperature. We performed numerical simulations at zero temperature for a frustrated spin-1 system on the basis of a J_1-J_2-J_3-K Heisenberg model[12] on a 16-points cluster as shown in Fig. 2a and described in the Methods section. Figure 2b shows the resulting phase diagram as a function of J_2 and J_3. K was set at 0.1 (repulsive) in order to suppress ordering tendencies on the small cluster. The parameter set for the simulations of the Raman and neutron data at finite temperature is indicated as a black dot.

In Fig. 3 we show the low-temperature data (Fig. 3a) along with the simulations (Fig. 3b). The energy scale for the simulations is given in units of J_1 which has been derived[12] to be 123 meV or 990 cm^{-1}, allowing a semi-quantitative comparison with the experiment. As already mentioned, the experimental A_{1g} and B_{2g} spectra are not dominated by spin excitations and we do not attempt to further analyze the continua extending to energies in
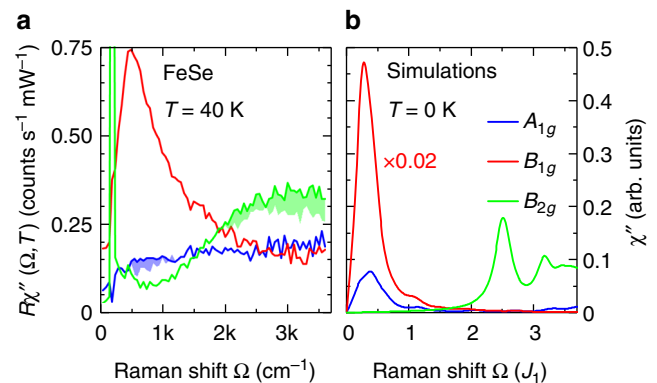

Fig. 3 Symmetry-resolved Raman spectra of FeSe for large energy shifts at low temperature. **a** Experimental results for symmetries as indicated at 40 K. The B_{1g} peak at 500 cm^{-1} dominates the spectrum. In A_{1g} and B_{2g} symmetry the electron-hole continua dominate the response, and the magnetic excitations yield only small additional contributions at approximately 700 and 3000 cm^{-1}, respectively. **b** Simulated Raman spectra at $T = 0$ K including only magnetic contributions. The A_{1g} and B_{1g} symmetries have peaks solely at low energies whereas the B_{2g} contributions are at high energies only. The B_{1g} response is multiplied by a factor of 0.02

excess of 1 eV, considering them a background. The opposite is true for B_{1g} symmetry, also borne out in the simulations. For the selected values of $J_1 = 123$ meV, $J_2 = 0.528J_1$, $J_3 = 0$, and $K = 0.1J_1$, the positions of the spin excitations in the three symmetries and the relative intensities are qualitatively reproduced. The choice of parameters is motivated by the previous use of the J_1-J_2 Heisenberg model, with $J_1 = J_2$ to describe the stripe phase of iron pnictides[20]. Here we use a value of J_2 smaller than J_1 to enhance competition between Néel and stripe orders when describing

FeSe. This approach and choice of parameters is strongly supported in a recent neutron scattering study[27].

The comparison of the different scattering symmetries, the temperature dependence, and our simulations indicate that the excitation at $500\,cm^{-1}$ is an additional scattering channel superimposed on the particle-hole continuum and fluctuation response, as shown in Supplementary Note 3 with Supplementary Figs. 3 and 4. Here we focus on the peak centered at $\sim500\,cm^{-1}$ which, in agreement with the simulations, originates from two-magnon excitations in a highly frustrated spin system, although the features below $500\,cm^{-1}$ also are interesting and were interpreted in terms of quadrupolar orbital fluctuations[29].

Temperature dependence. It is enlightening to look at the B_{1g} spectra across the whole temperature range as plotted in Fig. 4. The well-defined two-magnon peak centered at $\sim500\,cm^{-1}$ in the low temperature limit loses intensity, and becomes less well-defined with increasing temperature up to the structural transition $T_s = 89.1$ K. Above the structural transition, the spectral weight continues to decrease and the width of the two-magnon feature grows, while the peak again becomes well-defined and the energy increases slightly approaching the high temperature limit of the study. What may appear as a gap opening at low temperature is presumably just the reduction of spectral weight in a low-energy feature at $\sim22\,cm^{-1}$. The intensity of this lower energy response increases with temperature, leading to a well-formed peak at an energy around $50\,cm^{-1}$ near the structural transition. Above the structural transition this feature rapidly loses spectral weight, hardens, and becomes indistinguishable from the two-magnon response in the high temperature limit. This low-energy feature develops in a fashion very similar to that found in $Ba(Fe_{1-x}Co_x)_2As_2$ for $x > 0$[33–35].

Now we compare the measurements with numerical simulations for the temperature dependence of the Raman B_{1g} susceptibility in Fig. 5a, b, respectively. For the simulations (Fig. 5b) we use the same parameters as at $T = 0$ (black dot in Fig. 3). At zero temperature the simulations show a single low energy B_{1g} peak around $0.3J_1$. As temperature increases, a weak shoulder forms on the low-energy side of the peak, and the whole peak softens slightly and broadens over the simulated temperature range. Except for the additional intensity at low energies, $\Omega < 200\,cm^{-1}$ (Fig. 5a), there is good qualitative agreement between
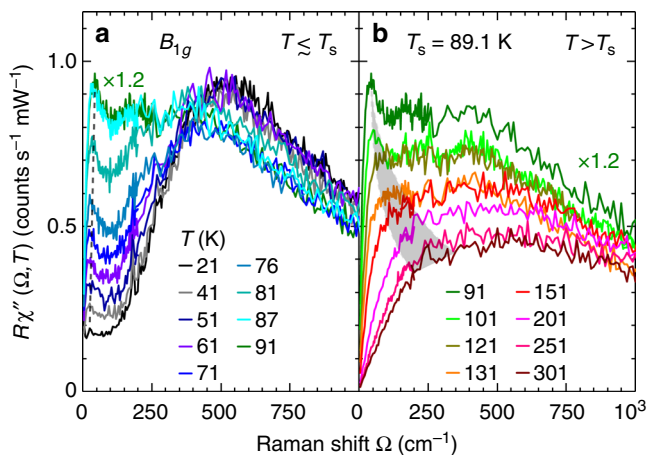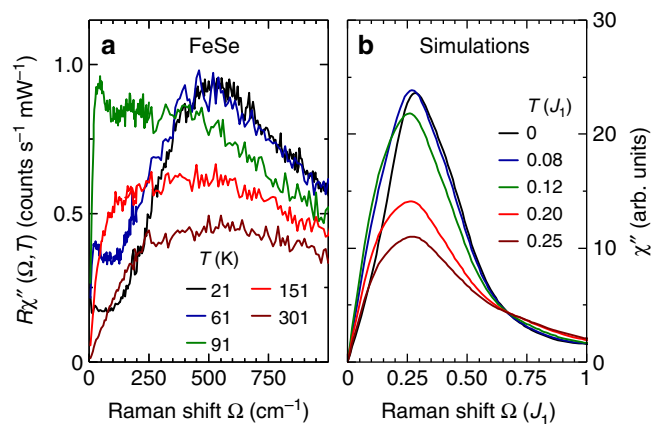

Fig. 5 Temperature dependence of the B_{1g} response. **a** Experimental spectra at selected temperatures as indicated. The spectra include several excitations the decomposition of which is shown in Supplementary Fig. 4. **b** Simulated Raman response at temperatures as indicated. Only magnetic excitations are included. The coupling constant was derived as $J_1 = 123$ meV in ref. [12]

theory and experiment. As shown in Supplementary Fig. 5 in Supplementary Note 4, a similar agreement between experiment and simulations is obtained for the temperature dependence in A_{1g} and B_{2g} symmetries, indicating that both the gain in intensity (blue shaded areas in Fig. 1) as well as the reduction in spectral weight in B_{2g} from 600 to $1900\,cm^{-1}$ (shaded red in Fig. 1d) can be attributed to the frustrated localized magnetism.

Connection to the spin structure factor. To support our explanation of the Raman data, we simulated the dynamical spin structure factor $S(\mathbf{q}, \omega)$ and compared the findings to results of neutron scattering experiments[27]. While clearly not observing long-range order, above the structural transition neutron scattering finds similar intensity at finite energy for several wave vectors along the line $(\pi, 0) - (\pi, \pi)$. Upon cooling, the spectral weight at these wave vectors shifts away from (π, π) to directions along $(\pi, 0)$, although the respective peaks remain relatively broad. In Fig. 6a, b we show the results of the simulations for two characteristic temperatures. As the temperature decreases, spectral weight shifts from (π, π) toward $(\pi, 0)$ in agreement with the experiment[27]. In Fig. 6c we show the evolution of the spectral weights around (π, π) and $(\pi, 0)$ in an energy window of $(0.4 \pm 0.1)J_1$ as a function of temperature, similar to the results shown in ref. [27]. In the experiment, the temperature where the integrated dynamical spin structure factor changes most dramatically is close to the structural transition. From our simulations, the temperature where similar changes occur in comparison to neutron scattering corresponds to the temperature at which the simulated B_{1g} response (Fig. 5) shows the most pronounced shoulder, and the overall intensity begins to decrease. Not surprisingly, the low-energy peak in the Raman scattering experiment is also strongest near the structural transition.

Fig. 4 Raman spectra in B_{1g} symmetry at temperatures **a** below and **b** above $T_s = 89.1$ K. The spectrum at 91 K appears in both panels for better comparison. The black dashed line in **a** and the gray shaded area in **b** indicate the approximate positions of the low-energy peak resulting from critical fluctuations. The peak centered close to $500\,cm^{-1}$ results from excitations of neighboring spins which are studied here. A tentative decomposition is shown in Supplementary Fig. 4

Discussion

The agreement of experiment with theory in both neutron and Raman scattering suggests that a dominant contribution to the FeSe spectra comes from frustrated magnetism of essentially local spins. The differences between the classes of ferro-pnictides and -chalcogenides, in particular the different degrees of itinerancy, may then originate in a subtle orbital differentiation across the families[1].
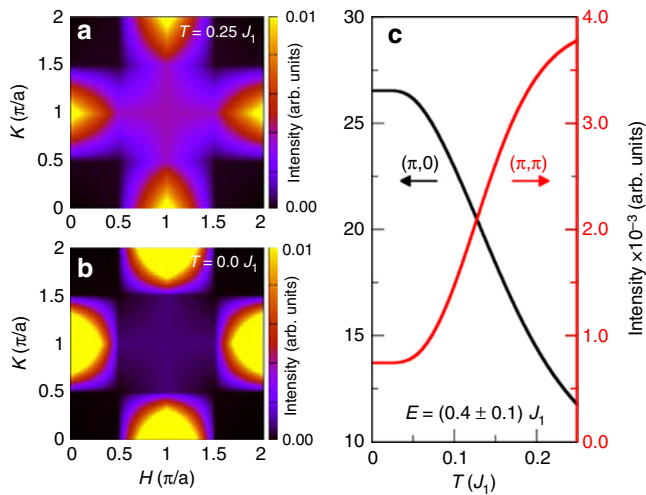
Fig. 6 Simulations of the dynamical structure factor $S(\mathbf{q}, \omega)$ of localized spin excitations integrated over an energy window of $(0.4 \pm 0.1)J_1$. **a, b** display cuts through the first Brillouin zone at $T = 0.25$ and $0J_1$, respectively. At high temperature there is intensity at (π, π) indicating a tendency toward Néel order. At low temperature the intensity at (π, π) is reduced and the stripe-like antiferromagnetism with $(\pi, 0)$ ordering wave vector becomes stronger. **c** $S(\mathbf{q}, \omega)$ integrated over an energy window $(0.4 \pm 0.1)J_1$ for fixed momenta (π, π) and $(\pi, 0)$ intensities as a function of temperature
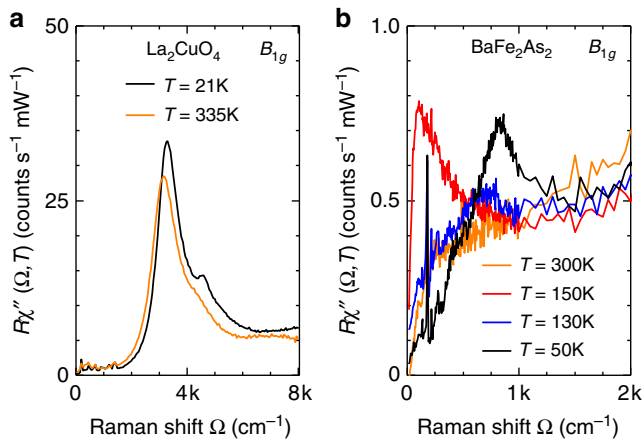
Fig. 7 Examples of localized and itinerant magnets. **a** B_{1g} Raman spectra of La$_2$CuO$_4$. From ref. [31]. **b** B_{1g} spectra of BaFe$_2$As$_2$ at four characteristic temperatures as indicated

If FeSe were frustrated, near such a phase boundary between magnetic states, then its behavior would be consistent with the observed sensitivity to intercalation[36,37], layer thickness[38], and pressure[39], which could affect the exchange interactions through the hopping. Relative to the theoretical results below 200 cm^{-1}, critical fluctuations of any origin, which are characterized by a diverging correlation length close to the transition, can neither be described nor distiguished in such a small cluster calculation. Here, only experimental arguments can be applied similar to those in ref. [35], but will not be further discussed, since they are not the primary focus of the analysis. A brief summary may be found in the Supplementary Note 3.

It is remarkable how clearly the Raman spectra of an SDW state originating from a Fermi surface instability and a magnet with local moments can be distinguiished. For comparison, Fig. 7

shows B_{1g} Raman spectra for La$_2$CuO$_4$ and BaFe$_2$As$_2$ at characteristic temperatures. La$_2$CuO$_4$ (Fig. 7a) is an example of a material with local moments on the Cu sites[30,31] having a Néel temperature of $T_N = 325$ K. The well-defined peak at ~$2.84J_1$[40,41] possesses a weak and continuous temperature dependence across T_N[32]. The origin of the scattering in La$_2$CuO$_4$ and other insulating cuprates[42] can thus be traced back to Heisenberg-type physics of local moments[43], which, for simplicity, need only include the nearest-neighbor exchange interaction J_1.

In contrast, most iron-based superconductors are metallic antiferromagnets in the parent state exhibiting rather different Raman signatures. In BaFe$_2$As$_2$ (Fig. 7b) abrupt changes are observed in B_{1g} symmetry upon entering the SDW state: the fluctuation peak below 100 cm^{-1} vanishes, a gap develops below some 500–600 cm^{-1}, and intensity piles up in the range 600–1500 cm^{-1} (ref. [22,44]), the typical behavior of an SDW or CDW[24] in weak-coupling, resulting from Fermi surface nesting. Yet, even for itinerant systems such as these, longer range exchange interactions can become relevant and lead to magnetic frustration[45].

In summary, the Raman response of FeSe was measured in all symmetries and compared to simulations of a frustrated spin-1 system. The experimental data were decomposed in order to determine which parts of the spectra originate from particle-hole excitations, fluctuations of local spins, and low energy critical fluctuations. Comparison of the decomposed experimental data with the simulations gives evidence that the dominant contribution of the Raman spectra comes from magnetic competition between $(\pi, 0)$ and (π, π) ordering vectors. These features of the Raman spectra, which agree qualitatively with a spin-only model, consist of a dominant peak in B_{1g} symmetry around 500 cm^{-1} along with a peak at similar energy but lower intensity in A_{1g} and at higher energy in B_{2g} symmetry. These results will likely help to unravel the mechanism behind the superconducting phase found in FeSe.

Methods

Experiment. The FeSe crystals were prepared by the vapor transport technique. Details of the crystal growth and characterization are described elsewhere[46]. Before the experiment the samples were cleaved in air and the exposure time was minimized. The surfaces obtained in this way have several atomically flat regions allowing us to measure spectra down to 5 cm^{-1}. At the tetragonal-to-orthorhombic transition T_s twin boundaries appear and become clearly visible in the observation optics. As described in detail by Kretzschmar et al.[35] the appearance of stripes can be used to determine the laser heating ΔT_L and T_s to be (0.5 ± 0.1) Km W^{-1} and (89.1 ± 0.2) K, respectively.

Calibrated Raman scattering equipment was used for the experiment. The samples were attached to the cold finger of a He-flow cryostat having a vacuum of ~5×10^{-5} Pa (5×10^{-7} mbar). For excitation we used a diode-pumped solid state laser emitting at 575 nm (Coherent GENESIS MX-SLM 577-500) and various lines of an Ar ion laser (Coherent Innova 304). The angle of incidence was close to 66° for reducing the elastic stray light entering the collection optics. Polarization and power of the incoming light were adjusted in a way that the light inside the sample had the proper polarization state and, respectively, a power of typically $P_a = 4$ mW independent of polarization. For the symmetry assignment we use the 1 Fe unit cell (axes x and y parallel to the Fe–Fe bonds) which has the same orientation as the magnetic unit cell in the cases of Néel or single-stripe order (4 Fe cell). The orthorhombic distortion is along these axes whereas the crystallographic cell assumes a diamond shape with the length of the tetragonal axes preserved. Because of the rotated axes in the 1 Fe unit cell the Fe B_{1g} phonon appears in the B_{2g} spectra. Spectra at low to medium energies were measured with a resolution $\sigma \approx 5$ cm^{-1} in steps of $\Delta\Omega = 2.5$ or 5 cm^{-1} below 250 cm^{-1} and steps of 10 cm^{-1} above where no sharp peaks need to be resolved. Spectra covering the energy range up to 0.5–1 eV were measured with a resolution $\sigma \approx 20$ cm^{-1} in steps of $\Delta\Omega = 50$ cm^{-1}.

Simulations. We use exact diagonalization to study a Heisenberg-like model on a 16-site square lattice, which contains the necessary momentum points and is small enough that exact diagonalization can reach high enough temperatures to find agreement with the temperature dependence in the experiment. This was solved

using the parallel Arnoldi method[47]. The Hamiltonian is given by

$$\mathcal{H} = \sum_{nn} \left[J_1 \mathbf{S}_i \cdot \mathbf{S}_j + K \left(\mathbf{S}_i \cdot \mathbf{S}_j \right)^2 \right] \\ + \sum_{2nn} J_2 \mathbf{S}_i \cdot \mathbf{S}_j + \sum_{3nn} J_3 \mathbf{S}_i \cdot \mathbf{S}_j \tag{1}$$

where $\mathbf{S}_i$ is a spin-1 operator reflecting the observation that the local moments of iron chalcogenides are close to $2\mu_B$[48]. The sum over nn is over nearest neighbors, the sum over 2nn is over next nearest neighbors, and the sum over 3nn is over next next nearest neighbors.

We determine the dominant order according to the largest static spin structure factor, given by

$$S(\mathbf{q}) = \frac{1}{N} \sum_l e^{i\mathbf{q} \cdot \mathbf{R}_l} \sum_i \left\langle \mathbf{S}_{\mathbf{R}_i + \mathbf{R}_l} \cdot \mathbf{S}_{\mathbf{R}_i} \right\rangle. \tag{2}$$

Due to the possible spontaneous symmetry breaking we adjust the structure factor by the degeneracy of the momentum. To characterize the relative strength of the dominant fluctuations we project the relative intensity of the dominant static structure factor onto the range [0, 1] using the following

$$\text{Intensity} = 1 - \frac{d_{\mathbf{q}_{sub}} S(\mathbf{q}_{sub})}{d_{\mathbf{q}_{max}} S(\mathbf{q}_{max})} \tag{3}$$

where $d_{\mathbf{q}}$ is the degeneracy of momentum $\mathbf{q}$, $\mathbf{q}_{max}$ is the momentum with the largest $d_{\mathbf{q}} S_{\mathbf{q}}$, and $\mathbf{q}_{sub}$ is the momentum with the second largest (subdominant) $d_{\mathbf{q}} S_{\mathbf{q}}$.

The Raman susceptibilities for B_{1g}, B_{2g}, and A_{1g} symmetries for non-zero temperatures were calculated using the Fleury-Loudon scattering operator[20] given by

$$\mathcal{O} = \sum_{i,j} J_{ij} \left(\widehat{\mathbf{e}}_{in} \cdot \widehat{\mathbf{d}}_{ij} \right) \left(\widehat{\mathbf{e}}_{out} \cdot \widehat{\mathbf{d}}_{ij} \right) \mathbf{S}_i \cdot \mathbf{S}_j \tag{4}$$

where J_{ij} are the exchange interaction values used in the Hamiltonian, $\widehat{\mathbf{d}}_{ij}$ is a unit vector connecting sites i and j and $\widehat{\mathbf{e}}_{in/out}$ are the polarization vectors. For the symmetries calculated we use the polarization vectors

$$\widehat{\mathbf{e}}_{in} = \tfrac{1}{\sqrt{2}}(\widehat{\mathbf{x}} + \widehat{\mathbf{y}}), \ \ \widehat{\mathbf{e}}_{out} = \tfrac{1}{\sqrt{2}}(\widehat{\mathbf{x}} + \widehat{\mathbf{y}}) \text{ for } A_{1g} \oplus B_{2g}, \\ \widehat{\mathbf{e}}_{in} = \widehat{\mathbf{x}}, \ \ \widehat{\mathbf{e}}_{out} = \widehat{\mathbf{y}} \text{ for } B_{2g}, \\ \widehat{\mathbf{e}}_{in} = \tfrac{1}{\sqrt{2}}(\widehat{\mathbf{x}} + \widehat{\mathbf{y}}), \ \ \widehat{\mathbf{e}}_{out} = \tfrac{1}{\sqrt{2}}(\widehat{\mathbf{x}} - \widehat{\mathbf{y}}) \text{ for } B_{1g}, \tag{5}$$

(where $\widehat{\mathbf{x}}$ and $\widehat{\mathbf{y}}$ point along the Fe–Fe directions). We use this operator to calculate the Raman response $R(\omega)$ using the continued fraction expansion[49], where $R(\omega)$ is given by

$$R(\omega) = -\frac{1}{\pi Z} \sum_n e^{-\beta E_n} \text{Im} \left(\langle \Psi_n | \mathcal{O}^\dagger \frac{1}{\omega + E_n + i\epsilon - \mathcal{H}} \mathcal{O} | \Psi_n \rangle \right) \tag{6}$$

with Z the partition function. The sum traverses over all eigenstates Ψ_n of the Hamiltonian $\mathcal{H}$ having eigenenergies $E_n < E_0 + 2J_1$ where E_0 is the ground state energy. The Raman susceptibility is given by $\chi''(\omega) = \frac{1}{2}[R(\omega) - R(-\omega)]$. The dynamical spin structure factor was calculated using the same method with $\mathcal{O}$ replaced with $S_{\mathbf{q}}^z = \frac{1}{\sqrt{N}} \sum_l e^{i\mathbf{q} \cdot \mathbf{R}_l} S_l^z$. **Note added in proof:** More details about the numerical study of the model can be found in ref. [50].

Data availability
Data are available upon reasonable request from the corresponding author.

References

1. Yin, Z. P., Haule, K. & Kotliar, G. Kinetic frustration and the nature of the magnetic and paramagnetic states in iron pnictides and iron chalcogenides. *Nat. Mater.* **10**, 932–935 (2011).
2. Georges, A., de' Medici, L. & Mravlje, J. Strong correlations from Hund's coupling. *Annu. Rev. Cond. Mat. Phys.* **4**, 137–178 (2013).
3. Si, Q., Yu, R. & Abrahams, E. High-temperature superconductivity in iron pnictides and chalcogenides. *Nat. Rev. Mater.* **1**, 16017 (2016).
4. Skornyakov, S. L., Anisimov, V. I., Vollhardt, D. & Leonov, I. Effect of electron correlations on the electronic structure and phase stability of FeSe upon lattice expansion. *Phys. Rev. B* **96**, 035137 (2017).
5. Li, S. et al. First-order magnetic and structural phase transitions in Fe$_{1+y}$Se$_x$Te$_{1-x}$. *Phys. Rev. B* **79**, 054503 (2009).
6. Johnston, D. C. The puzzle of high temperature superconductivity in layered iron pnictides and chalcogenides. *Adv. Phys.* **59**, 803 (2010).
7. Yi, M., Zhang, Y., Shen, Z.-X. & Lu, D. Role of the orbital degree of freedom in iron-based superconductors. *npj Quantum Mater.* **2**, 57 (2017).
8. Baek, S.-H. et al. Orbital-driven nematicity in FeSe. *Nat. Mater.* **14**, 210–214 (2014).
9. Taylor, A. E. et al. Absence of strong magnetic fluctuations in FeP-based systems LaFePO and Sr$_2$ScO$_3$FeP. *J. Phys. Condens. Matter* **25**, 425701 (2013).
10. Mazin, I. I. & Johannes, M. D. A key role for unusual spin dynamics in ferropnictides. *Nat. Phys.* **5**, 141 (2009).
11. Stadler, K. M., Yin, Z. P., von Delft, J., Kotliar, G. & Weichselbaum, A. Dynamical mean-field theory plus numerical renormalization-group study of spin-orbital separation in a three-band Hund metal. *Phys. Rev. Lett.* **115**, 136401 (2015).
12. Glasbrenner, J. K. et al. Effect of magnetic frustration on nematicity and superconductivity in iron chalcogenides. *Nat. Phys.* **11**, 953–958 (2015).
13. Baum, A. et al. Interplay of lattice, electronic, and spin degrees of freedom in detwinned BaFe$_2$As$_2$: a Raman scattering study. *Phys. Rev. B* **98**, 075113 (2018).
14. Anisimov, V. I., Nekrasov, I. A., Kondakov, D. E., Rice, T. M. & Sigrist, M. Orbital-selective Mott-insulator transition in Ca$_{2-x}$Sr$_x$RuO$_4$. *Eur. Phys. J. B* **25**, 191–201 (2002).
15. de'Medici, L., Hassan, S. R., Capone, M. & Dai, X. Orbital-selective Mott transition out of band degeneracy lifting. *Phys. Rev. Lett.* **102**, 126401 (2009).
16. de' Medici, L. Hund's induced fermi-liquid instabilities and enhanced quasiparticle interactions. *Phys. Rev. Lett.* **118**, 167003 (2017).
17. Yi, M. et al. Observation of universal strong orbital-dependent correlation effects in iron chalcogenides. *Nat. Commun.* **6**, 7777 (2015).
18. Venturini, F. et al. Observation of an unconventional metal-insulator transition in overdoped CuO$_2$ compounds. *Phys. Rev. Lett.* **89**, 107003 (2002).
19. Devereaux, T. P. & Hackl, R. Inelastic light scattering from correlated electrons. *Rev. Mod. Phys.* **79**, 175 (2007).
20. Chen, C.-C., Jia, C. J., Kemper, A. F., Singh, R. R. P. & Devereaux, T. P. Theory of Two-Magnon Raman Scattering in Iron Pnictides and Chalcogenides. *Phys. Rev. Lett.* **106**, 067002 (2011).
21. Okazaki, K., Sugai, S., Niitaka, S. & Takagi, H. Phonon, two-magnon, and electronic Raman scattering of Fe$_{1+y}$Te$_{1-x}$Se$_x$. *Phys. Rev. B* **83**, 035103 (2011).
22. Sugai, S. et al. Spin-density-wave gap with Dirac nodes and two-magnon Raman scattering in BaFe$_2$As$_2$. *J. Phys. Soc. Jpn.* **81**, 024718 (2012).
23. Chauvière, L. et al. Raman scattering study of spin-density-wave order and electron-phonon coupling in Ba(Fe$_{1-x}$Co$_x$)$_2$As$_2$. *Phys. Rev. B* **84**, 104508 (2011).
24. Eiter, H.-M. et al. Alternative route to charge density wave formation in multiband systems. *Proc. Natl Acad. Sci. USA* **110**, 64–69 (2013).
25. Yang, Y.-X. et al. Temperature-induced change in the Fermi surface topology in the spin density wave phase of Sr(Fe$_{1-x}$Co$_x$)$_2$As$_2$. *Phys. Rev. B* **89**, 125130 (2014).
26. Wang, F., Kivelson, S. A. & Lee, D.-H. Nematicity and quantum paramagnetism in FeSe. *Nat. Phys.* **11**, 959–963 (2015).
27. Wang, Q. et al. Magnetic ground state of FeSe. *Nat. Commun.* **7**, 12182 (2016).
28. Rahn, M. C., Ewings, R. A., Sedlmaier, S. J., Clarke, S. J. & Boothroyd, A. T. Strong $(\pi, 0)$ spin fluctuations in β−FeSe observed by neutron spectroscopy. *Phys. Rev. B* **91**, 180501 (2015).
29. Massat, P. et al. Charge-induced nematicity in FeSe. *Proc. Natl Acad. Sci. USA* **113**, 9177–9181 (2016).
30. Sulewski, P. E., Fleury, P. A., Lyons, K. B. & Cheong, S.-W. Observation of chiral spin fluctuations in insulating planar cuprates. *Phys. Rev. Lett.* **67**, 3864 (1991).
31. Muschler, B. et al. Electron interactions and charge ordering in CuO$_2$ compounds. *Eur. Phys. J. Spec. Top.* **188**, 131 (2010).
32. Knoll, P., Thomsen, C., Cardona, M. & Murugaraj, P. Temperature-dependent lifetime of spin excitations in RBa$_2$Cu$_3$O$_6$ (R = Eu, Y). *Phys. Rev. B* **42**, 4842–4845 (1990).
33. Choi, K.-Y. et al. Lattice and electronic anomalies of CaFe$_2$As$_2$ studied by Raman spectroscopy. *Phys. Rev. B* **78**, 212503 (2008).
34. Gallais, Y. et al. Observation of incipient charge nematicity in Ba(Fe$_{1-x}$Co$_x$)$_2$As$_2$. *Phys. Rev. Lett.* **111**, 267001 (2013).
35. Kretzschmar, F. et al. Critical spin fluctuations and the origin of nematic order in Ba(Fe$_{1-x}$Co$_x$)$_2$As$_2$. *Nat. Phys.* **12**, 560–563 (2016).
36. Burrard-Lucas, M. et al. Enhancement of the superconducting transition temperature of fese by intercalation of a molecular spacer layer. *Nat. Mater.* **12**, 15–19 (2013).
37. Zhang, A.-M. et al. Superconductivity at 44 K in K intercalated FeSe system with excess Fe. *Sci. Rep.* **3**, 1216 (2013).
38. Ge, J.-F. et al. Superconductivity above 100 K in single-layer FeSe films on doped SrTiO$_3$. *Nat. Mater.* **14**, 285–289 (2015).

39. Medvedev, S. et al. Electronic and magnetic phase diagram of β-Fe$_{1.01}$Se with superconductivity at 36.7 K under pressure. *Nat. Mater.* **8**, 630 (2009).

40. Canali, C. M. & Girvin, S. M. Theory of Raman scattering in layered cuprate materials. *Phys. Rev. B* **45**, 7127–7160 (1992).

41. Weidinger, S. A. & Zwerger, W. Higgs mode and magnon interactions in 2D quantum antiferromagnets from Raman scattering. *Eur. Phys. B* **88**, 237 (2015).

42. Chelwani, N. et al. Magnetic excitations and amplitude fluctuations in insulating cuprates. *Phys. Rev. B* **97**, 024407 (2018).

43. Fleury, P. A. & Loudon, R. Scattering of light by one- and two-magnon excitations. *Phys. Rev.* **166**, 514 (1968).

44. Chauvière, L. et al. Impact of the spin-density-wave order on the superconducting gap of Ba(Fe$_{1-x}$Co$_x$)$_2$As$_2$. *Phys. Rev. B* **82**, 180521 (2010).

45. Yildirim, T. Frustrated magnetic interactions, giant magneto-elastic coupling, and magnetic phonons in iron-pnictides. *Phys. C.* **469**, 425 (2009).

46. Böhmer, A. E. et al. Lack of coupling between superconductivity and orthorhombic distortion in stoichiometric single-crystalline FeSe. *Phys. Rev. B* **87**, 180505 (2013).

47. Sorensen, D., Lehoucq, R. & Yang, C. *ARPACK Users' Guide: Solution of Large-Scale Eigenvalue Problems with Implicitly Restarted Arnoldi Methods.* (Siam, Philadelphia, 1998).

48. Gretarsson, H. et al. Revealing the dual nature of magnetism in iron pnictides and iron chalcogenides using x-ray emission spectroscopy. *Phys. Rev. B* **84**, 100509 (2011).

49. Dagotto, E. Correlated electrons in high-temperature superconductors. *Rev. Mod. Phys.* **66**, 763 (1994).

50. Ruiz, H., Wang, Y., Moritz, B. & Devereaux, T. P. Frustrated magnetism from local moments in FeSe. Preprint at https://arxiv.org/abs/1812.09609 (2018).

Author contributions

A.B., T.B. and R.H. conceived the experiment. B.M. and T.P.D. conceived the ED analysis. P.A. and T.W. synthesized and characterized the samples. A.B., N.L., T.B. and R.H. A. performed the Raman scattering experiment. H.N.R. and Y.W. coded and performed the ED calculations. A.B., H.N.R., N.L., B.M. and R.H. analyzed and discussed the data. A.B., H.N.R., N.L., Z.P., B.M., T.P.D. and R.H. wrote the paper. All authors commented on the manuscript.

Additional information

Supplementary information accompanies this paper at https://doi.org/10.1038/s42005-019-0107-y.

Competing interests: The authors declare no competing interests.

Reprints and permission information is available online at http://npg.nature.com/reprintsandpermissions/

Publisher's note: Springer Nature remains neutral with regard to jurisdictional claims in published maps and institutional affiliations.